Nature of pressure waves induced by a high-speed train travelling through a tunnel

Pierre Ricco [a,b,*], Arturo Baron [b], Paolo Molteni [b]

[a] *Environmental and Applied Fluid Dynamics Department, von Kármán Institute for Fluid Dynamics, 72, Chaussée de Waterloo, B-1640 Rhode Saint Genèse, Belgium*

[b] *Dipartimento di Ingegneria Aerospaziale, Politecnico di Milano, via La Masa, 34 - 20156 Milano, Italy*

---

* Corresponding author. Present address: Institute for Mathematical Sciences, Imperial College London, 53 Prince's Gate, London SW7 2PG, United Kingdom.
Email address: pierre.ricco@imperial.ac.uk (Pierre Ricco).
URL: http://www.ma.ic.ac.uk/~par/ (Pierre Ricco).

Preprint submitted to J. Wind Eng. Ind. Aerodyn. *26 March 2009*

Abstract

Published as Pierre Ricco, Arturo Baron, Paolo Molteni *Nature of pressure waves induced by a high-speed train travelling through a tunnel* Journal of Wind Engineering and Industrial Aerodynamics, Volume 95, Issue 8, August 2007, Pages 781-808.

The pressure waves generated by a train entering and running through a tunnel are studied experimentally and numerically with the aim of gaining a solid understanding of the flow in the standard tunnel geometry and in the configuration with airshafts along the tunnel surface. Laboratory experiments were conducted in a scaled facility where train models travelled at a maximum velocity of about 150 km/h through a 6-meter-long tunnel. The flow was simulated by a one-dimensional numerical code modified to include the effect of the separation bubble forming near the train head. The numerical simulations reproduced well the experimental results. We tested the influence of the train cross-sectional shape and length on the compression wave produced by the vehicle entering the confined area. The cross-section shape was not found to be influential as long as the blockage ratio, namely the ratio between the train and tunnel cross-sectional areas, is constant. The pressure waves are one-dimensional sufficiently downwind of the tunnel mouth, thus validating the comparison between the experimental and computational results. It is further shown that the numerical code can satisfactorily reproduce the pressure variations for the case with airshaft apertures along the tunnel surface.

Key words: Pressure waves, high-speed trains, tunnel aerodynamics, airshafts, one-dimensional flow

1 Introduction

The railway industry has recently undergone a flourishing period of improvement and innovation, especially in the high-speed vehicle technology, due to the growing necessity of an efficient transport system competing with airplane and automobile vehicles. In the last twenty-five years, railroad engineering research has led to vehicles travelling at speeds as high as 300 km/h (Mach number M=0.24), especially in densely populated areas, such as Western Europe, Japan and South Korea. Technological advancements have grown together with engineering problems such as the increment of aerodynamic drag [1],[2],[3],[4],[5],[6] and the stability of the vehicle. Aerodynamic noise is a major concern in high-speed operating conditions, whereas noise due to wheel rolling is a disturbing factor at low speeds.

Research efforts have been significantly directed to the design of high-speed trains running through tunnels because of the need to travel at high velocity notwithstanding the presence of environmental obstacles, such as mountains or rivers. Issues related to the aerodynamics in open spaces become even more involved when the vehicle runs through a gallery since compression and expansion waves are generated when the train passes an opening or encounters a change in the tunnel section [7]. These waves produce discomfort for the passengers and give rise to further complications such as the possible damage of the vehicle and the release of spherical micro-pressure waves from the tunnel apertures, which causes environmental annoyance [8],[9],[10]. One of the factors affecting the compression effect is the blockage ratio. This quantity must be reduced bearing in mind constraints such as the minimal cross-sectional area of the vehicle and the costs related to the increment of the tunnel diameter. Other design problems aimed at reducing the pressure intensity concern the shape of the nose [11],[12],[13],[14] and of the cross section [15]. The tunnel geometry has also been the subject of extensive investigations. Modifications have been applied to the tunnel entrance and exit, in the form of vented [16],[17],[13] or flared and enlarged portals [13],[18],[19],[20]. Airshaft apertures on the tunnel surface have also been used [19],[21],[22],[23],[24],[25]. The latter may also serve the purpose of ventilation of polluted air at low costs [26],[27]. Railway tunnels in partial vacuum have also been studied because they offer a reduction of pressure intensity, while guaranteeing contained building costs [28],[29]. The effect of the train position with respect to the tunnel axis has been studied by [2], who showed that the train off-centering produces a more intense gradient in the initial pressure rise.

As a first step to gain a sound understanding of the flow, we study the initial pressure rise and the pressure periodicity inside the tunnel. Once these basic physical mechanisms have been addressed, we focus on three key objectives:

- We simulate the flow with a one-dimensional code and we find good agreement with the experimental pressure distribution inside the tunnel when no *recirculation region* is present around the train head. However, when less aerodynamically-designed train models are employed, the local separation generates an additional pressure growth, which is not captured by the simulations. The first objective is to modify the code with a simple model to account for this effect. The approach is further verified by axisymmetric computations carried out with the commercial code Fluent. To our knowledge, this is the first study targeted at including the effect of the separation region in a one-dimensional code.
- We aim at investigating experimentally the influence of the *train cross-sectional shape* on the pressure distribution for a given blockage ratio and train nose geometry. We use trains with circular and squared cross sections. This analysis was also motivated by a previous study [15], which shows differences in the pressure gradients for cases with the same blockage ratio, but with different cross-sections. No definite conclusions can be drawn from these results on the effect of cross-section as the train models were off-centered with respect to the tunnel axis. The discrepancies could be due to the viscous effects on the tunnel walls. Our analysis is relevant to confirm the validity of one-dimensional numerical codes.
- The third task is to study experimentally the effect of the *train length* on the initial pressure rise. The problem was first numerically addressed by [30] and has never been studied in the laboratory.

We end the paper by presenting results on the influence of airshaft apertures on the tunnel surface which have the purpose of alleviating the intensity of the pressure variations. We show that our numerical code is capable of reproducing these experimental results.

The article is organized as follows. The laboratory facility and experimental procedures are presented in section §2. The numerical issues are described in section §3, with focus on the separation bubble model. Section §4 discusses the pressure pattern in the standard tunnel geometry, presenting the effects of the train nose, cross-sectional shape, length and airshaft apertures. Section §5 is devoted to the summary.

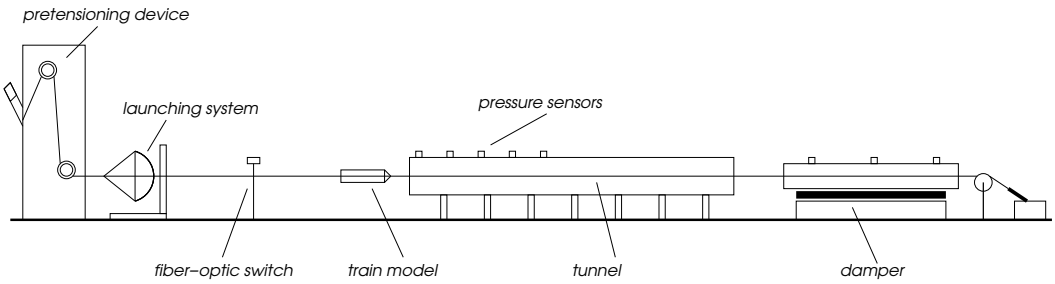

Fig. 1. Schematic of tunnel, launching system and pre-tensioning device.

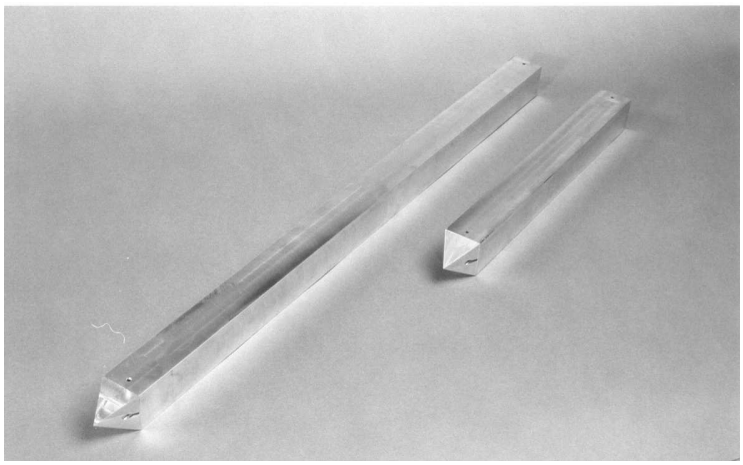

Fig. 2. Train models with squared cross-sectional shape.

2 Experimental apparatus and procedures

The experimental study was conducted at the von Kármán Institute for Fluid Dynamics. This section describes the facility (see figure 1) and the experimental procedures. Other train-tunnel scaled facilities are located at the British Rail Research [31], at the Civil Engineering Department at the University of Dundee [32], at the Railway Technical Research Institute [7], at the Nationaal Lucht-en Ruimtevaartlaboratorium [33],[34], at the Laboratoire de Combustion et de Détonique [35] and at the Ecole National Supérieure de Mécanique et d'Aérotechnique [36].

The train models had both circular and squared sections. The circular models measured 300 and 600 mm in length and 38 mm in diameter. They had conical noses with angles α=30°, 60° and 90° between the axis and the directrix. They were made of plastic and the noses of wood. The squared-section models, shown in figure 2, were made of aluminum and had the same length as the circular trains. The nose had a pyramidal shape with a 30° angle between the axis and the apothem of the lateral triangle. The side of the squared section was 33.7 mm long and the blockage ratio β=0.1475 was the same as that of the circular models.

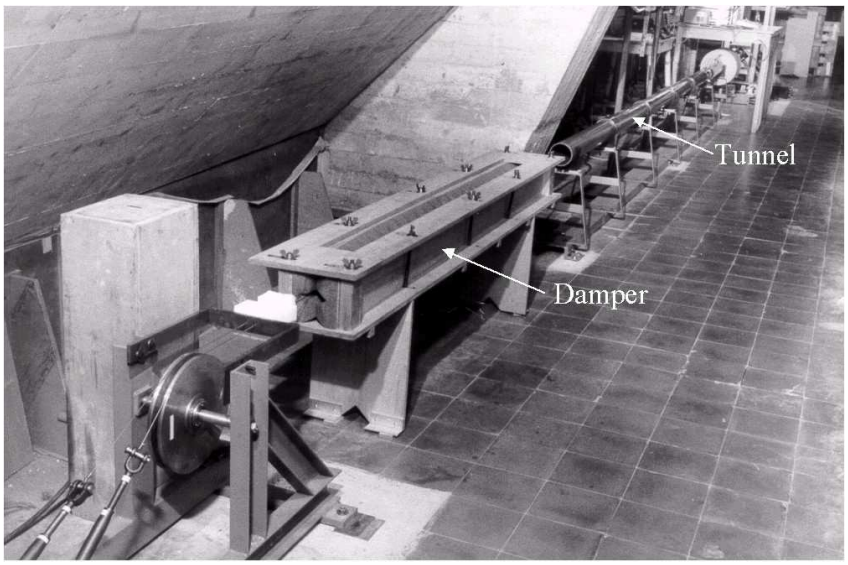

Fig. 3. Tunnel and damping system.

The 1:87-scaled setup consisted of a launching mechanism, a 6-meter-long tunnel and a damping system to block the vehicle after the tunnel exit (see figure 3). The models could reach a maximum velocity of 150 km/h (42 m/s). The tunnel had a uniform, circular cylindrical section of 99 mm in diameter with a thickness of 5 mm. It was composed of six identical 1-meter-long plastic tubes, which were properly assembled to avoid any discontinuity along the confined area. Four circular apertures of 20 mm in diameter were located along the tunnel length at l=17, 300, 600 and 900 mm from the entrance. The ratio between one aperture area and the tunnel area (aperture ratio $\mathcal{A}$) was about 0.04. Their purpose was twofold: they provided the access for the pressure sensors and functioned as airshafts for alleviating the pressure intensity when left open. At l=1180 mm, three such apertures were positioned at 120° from one another to study the pressure waves in a section perpendicular to the tunnel axis. The models ran on two parallel 2 mm diameter steel cables which were stretched along the tunnel axis. They were chosen as thin as possible not to influence the pressure field, but thick enough to be safely pulled taut and allow the models to smoothly slide along. The ratios between this thickness and the train and tunnel diameters were comparable with the ones of other rigs in use [7],[57]. The cables were cleaned with alcohol and covered with a lubricant before each experiment. Four Teflon guiding rings were inserted in the nose and in the tail to permit the contact with the cables. They were regularly replaced due to deterioration.

A pre-tensioning device positioned behind the launching mechanism was used to pull the cables taut. The crossbow-like launching mechanism served the purpose of propelling the model at high speed through the tunnel. It operated by means of two elastic bands stretched by four limbs connected to an electric motor. An electronic switch automatically stopped the engine when the tension

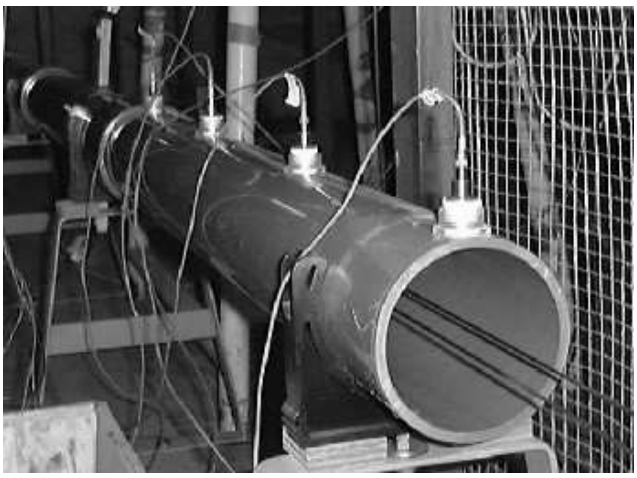

Fig. 4. Tunnel entrance and pressure transducers.

to launch the model at the required velocity was reached.

The damping system had the function of bringing the model to rest upon its exit from the tunnel. The kinetic energy was dissipated by friction inside the system. The damper measured about 2 m in length, 200 mm in height and 300 mm in width and it was located at a distance of about 1 m from the exit of the tunnel. It was composed of two inclined wooden plates internally covered with synthetic foam. These plates were adjusted to form a converging angle to provide a gradual resistance to the train. The foam was substituted twice during the experiments.

The static pressure was measured along the initial part of the tunnel by flush-mounted PCB Piezotronics microphones PCB106B50 (see figure 4). They measured a peak frequency of 40 kHz and static pressure changes up to 3448 kPa with a resolution of 0.48 Pa. A CA250 Precision Calibrator was used, which provided a nominal tone of 250 Hz at 114±0.1 dB with a reference value of 20 μPa. The uncertainty analysis accounted for the resolution of the PCB transducers and the errors of the amplifiers, the filters, the acquisition card and the calibrator. The errors of the measurement chain were estimated to 0.1 mV and the calibration errors to 0.1 Pa. The total uncertainty was about 2%.

The test producing the most intense pressure fluctuations, i.e. the short train with flat nose travelling at 140 km/h (38.9 m/s), was run to estimate the low-pass frequency of the filters and the sampling frequency of the acquisition board. For this test case, 2048 data points were acquired with the filter and sampling frequencies set to 12 kHz and 30 kHz, respectively. Noise was relevant for frequencies higher than ∼2.5 kHz. The filter was set to the lowest frequency allowed by our acquisition system higher than this value (3 kHz). The sampling frequency was 7.5 kHz to meet the Nyquist criterion [37].

The velocity of the model was measured by two photoelectric fiber-optic

switches (model WLL160 by Sick Optic-Electronic), located at 880 mm ahead of the tunnel entrance and at l=1180 mm. The first switch was located at about 1.5 m from the launching device to guarantee that the effect of the pressure waves produced by the initial acceleration of the model was negligible near the tunnel mouth [7]. Each switch consisted of a transmitter emitting a light beam perpendicularly to the cables. When the running train obstructed the beam, the transmitter sent a maximum voltage value as output to the acquisition system. After the passage of the train, the system received zero voltage as a signal. The velocity was calculated as the ratio between the train length and the time of the signal obstruction. It decreased by only 2% between the two locations. This allowed a valuable comparison with the computational results for which the train velocity was assumed constant. The first fiber-optic switch also triggered the data acquisition for the pressure measurements.

3 Physical and numerical model

The flow generated by a train travelling inside a tunnel is characterized by strong unsteadiness caused by the propagation and reflection of pressure waves. The effects of compressibility must be taken into account to study the flow, although the Mach number based on the train velocity V is relatively small ($M\approx0.12$). The reason for this lies in the two time scales being involved. The first scale is the time taken by the train to enter (or leave) the tunnel and the second one is the time for a pressure wave to travel the tunnel length at the speed of sound. Compressibility is important due to the unsteadiness when these scales are of the same order of magnitude. This form of compressibility is thus not relevant when the latter scale is much smaller than the former one. In this case the pressure disturbances generated by the vehicle entering (or leaving) the tunnel can be assumed to transmit instantaneously ([38] at page 450). The same concept is also elucidated by [39] at page 169, where it is shown that one must operate in the framework of compressible flows when $f^2 L_{tunnel}/a^2 \ll 1$, where f is a measure of the dominant frequency ($f=V/L_{train}$), L_{train} is the train length, L_{tunnel} is the tunnel length, and a the speed of sound. This expression translates into $M^2 L_{tunnel}/L_{train} \ll 1$. For example, a typical flow for which M=0.2 and $L_{tunnel}=5L_{train}$ must be treated as compressible. The requirement for incompressibility $M^2 \ll 1$ is only valid when one time scale controls the flow [1] .

[1] These incompressibility conditions are also based on the gravity forces being discarded (in laboratory experiments and in full-scale systems with atmospheric variations not exceeding a few hundred meters) and on negligible internal dissipative heating and heat conduction. These requirements are generally fulfilled when studying high-speed trains running through galleries.

The flow under study is also three–dimensional and turbulent. However, as confirmed in section §4.5, the pressure waves propagating inside long tunnels are essentially planar, being the distribution of the fluid dynamic variables often nearly uniform in each tunnel section. Three-dimensional effects must be considered near the tunnel portals and the train extremities. Accurate flow predictions are obtained by a one–dimensional approximation, provided that suitable corrective coefficients are employed to capture the local three–dimensional features. These coefficients are described in [41] at page 370.

3.1 Governing equations

The quasi one–dimensional unsteady compressible flow of a viscous fluid is governed by the equations of conservation of mass, momentum and energy in which the variables are assumed to be uniform in the tunnel cross section and to only depend on the axial coordinate x. These equations are written in an integral form for a varying control volume $\Omega(t)$ of surface $\Sigma(t)$ as:

$$\frac{d}{dt}\int\limits_{\Omega(t)} \mathbf{w}\, d\Omega + \oint\limits_{\Sigma(t)} \mathbf{f}\, d\Sigma = \int\limits_{\Omega(t)} \mathbf{s}\, d\Omega \,, \tag{1}$$

where the vector of the conservative variables $\mathbf{w}$, the vector of the convective fluxes $\mathbf{f}$ and the source vector $\mathbf{s}$ are:

$$\mathbf{w} = \{\rho, \rho u, E\}\,, \quad \mathbf{f} = \left\{\rho u, \rho u^2 + p, (E+p)u + k\ \partial T/\partial x\right\},$$

$$\mathbf{s} = \left\{ \begin{array}{c} 0 \\ \dfrac{1}{A}\left[p\dfrac{\partial A}{\partial x} - C_{f_g}\dfrac{1}{2}\rho u|u|\mathcal{P}_g - C_{f_t}\dfrac{1}{2}\rho(u-V)|u-V|\mathcal{P}_t\right] \\ \dfrac{1}{A}\left[-pV\dfrac{\partial A}{\partial x} - C_{f_t}\dfrac{1}{2}\rho(u-V)|u-V|\mathcal{P}_t V\right] + \dot{Q} \end{array} \right\},$$

where ρ is the air density, u is the air velocity, $E{=}\rho e{+}\frac{1}{2}\rho u^2$ is the total energy per unit volume, e indicates the internal energy per unit mass, p is the air pressure, T is air temperature, and k is the air thermal conductivity. The source vector $\mathbf{s}$ originates from:

- the one-dimensional approximation of the variation of the free cross section $A(x,t)$ due to the tunnel cross-sectional area (uniform in the present case) and to the running train;
- the viscous forces, which originate from the interactions between the fluid and the train and the tunnel walls, where $\mathcal{P}_g$ (resp. $\mathcal{P}_t$) is the perimeter of

the tunnel (resp. train) cross section and C_{f_g} (resp. C_{f_t}) is the skin friction coefficient of the tunnel wall (resp. train body);
- the thermal exchange, where $\dot{Q}$ is the heat power per unit volume.

The thermodynamic state equations of air (assumed to behave as an ideal gas) are used: $p{=}\rho RT$, $e{=}C_vT$, where C_v is the specific heat at constant volume and R is the ideal gas constant.

The spatial discretization is carried out by a cell–centered finite volume method. Numerical stability is guaranteed by second-order numerical dissipation terms scaled with an empirical coefficient. The train motion is simulated by the time and space variation of the cell volumes and interfaces. The flux terms are computed by considering the instantaneous free cross sections of the volume interfaces. A Jameson–like centered scheme [40] was used for the convective terms, in which time integration is based on a five–stage Runge–Kutta method. The grid spacing was equal to 1/20 of the tunnel diameter D_{tunnel} and CFL=2. The adiabatic wall condition, a temperature of 293 K and the standard pressure of 101325 Pa were used. The nose coefficients were 1.006 and 1.013 for the $\alpha{=}60°$ and $\alpha{=}90°$ case, respectively. The tail coefficient was 0.995 for both models (see [41] for definition of coefficients).

The airshafts are simulated as connections between two one–dimensional grids. The surface integrals in (1) are modified to take into account the secondary fluxes through $\Sigma(t)$ due to the airshafts. The apertures are modelled as short ducts (length to diameter ratio equal to one) connected with the tunnel. Local head losses in the junctions between the main tunnel and the airshafts are derived from [42] at page 179.

The reliability of the code has been widely tested by comparing the results with analytical solutions of compressible flows, such as flows in shock tubes or with acoustic waves [41], and with experimental data for railway tunnel configurations [43],[44],[45]. For more details one should refer to [10] and [41]. Other one-dimensional models are found in [46] and [47].

3.2 Separation bubble model

Noses with $\alpha{>}30°$ force a local boundary layer separation past the junction between the nose and the train body. This effect is not present for noses with $\alpha{\leq}30°$. This recirculation region is also called *separation bubble*, which is followed by the boundary layer reattachment and by transition to turbulence. The bubble primarily affects the amplitude of the head-induced pressure wave and less significantly its gradient (see section §4.4). In figure 5, a measured pressure trend is compared with numerical results obtained with and without the corrective separation bubble model. A notable discrepancy occurs at

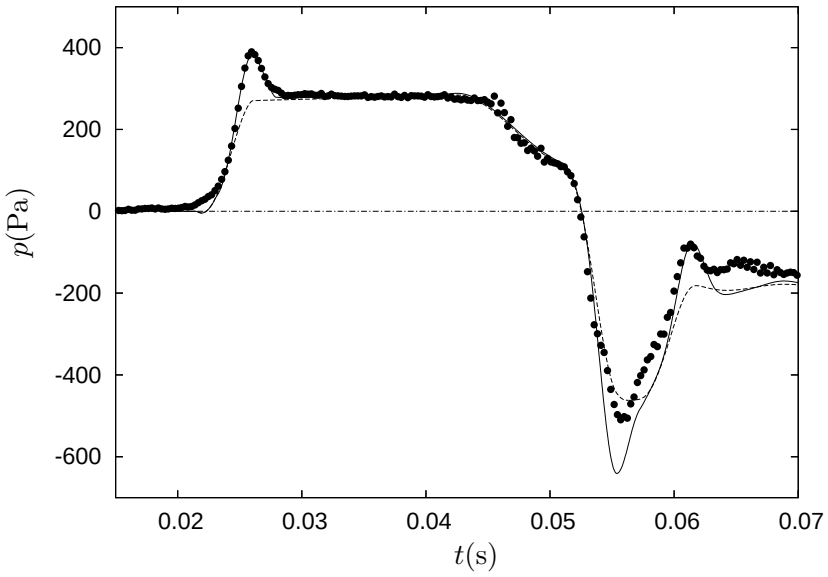

Fig. 5. Pressure pattern at l=900 mm for long train with α=60° travelling at 110 km/h (30.6 m/s). Comparison between experimental (•) and numerical data with (—) and without (– –) the separation bubble model. Every other experimental data point is shown for clarity.

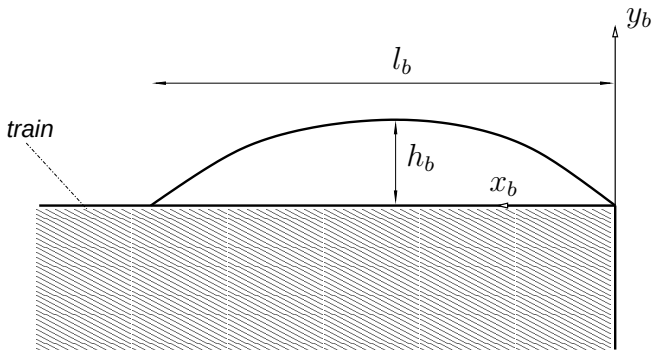

Fig. 6. Schematic of separation bubble on train body.

t≈0.026 s when the model is not used, because the separation can not be accounted for by a one-dimensional approximation.

The model is simple because separation past high-angle conical or pyramidal heads is largely independent from the Reynolds number and β. The recirculation region has been simulated by the addition of the local bubble thickness to the train head geometry (see figure 6). We assumed a sinusoidal shape: y_b=$h_b \sin(\pi x_b/l_b)$, where h_b is bubble height and l_b is its length. We kept the ratio h_b/l_b fixed (=1/5) and iteratively varied h_b until the initial pressure rise obtained numerically agreed with the experimental data to a specified level of accuracy. The length l_b is much less influential than h_b, so that h_b/l_b=1/5 for all the simulations. The values of h_b was kept constant for simulations involving the same train geometry. For α=60°, h_b=3.1 mm (8.2% of train diameter

D_{train}), while, for α=90°, h_b=5.2 mm (14% of D_{train}). The peak at $t\approx$0.062 s is also predicted more accurately.

3.3 Axisymmetric computations

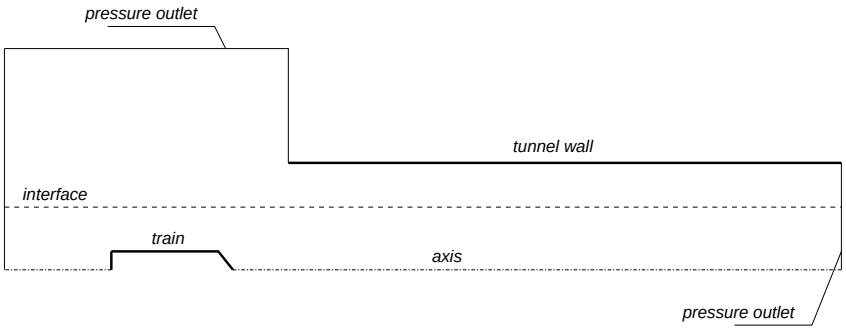

Fig. 7. Sketch of the computational domain (not to scale).

Axisymmetric computations have been performed with Fluent to confirm the values of h_b and l_b obtained in section §3.2. We have studied the cases with α=30°, 60°, 90° with V=38.9 m/s, 42.5 m/s, 38.9 m/s, respectively. The sliding mesh technique was used, in which two independent grids move relatively to each other along an interface parallel to the symmetry axis (see figure 7). The stationary grid is fixed with the tunnel and the moving one with the train. An unsteady, compressible, turbulent calculation was carried out using a RNG $k-\epsilon$ turbulence model employing a second-order upwind discretization scheme. As the separation past the nose was studied, the computational domain was limited to 1 m ($\approx 10 D_{tunnel}$) upwind and downwind of the tunnel entrance. A grid-independence analysis was performed, which resulted in about 15000 cells being employed. The closest point to the train surface was at about $50\nu/u_\tau$, where u_τ is the wall friction velocity and ν is the kinematic viscosity of air. The Fluent standard wall function was used, which approximates the mean velocity profile with the logarithmic law-of-the-wall and the linear stress-strain relationships. The computations were carried out with a time step of 10^{-5} s over a time interval of 0.015 s, with the train head starting 0.2 m from the tunnel entrance.

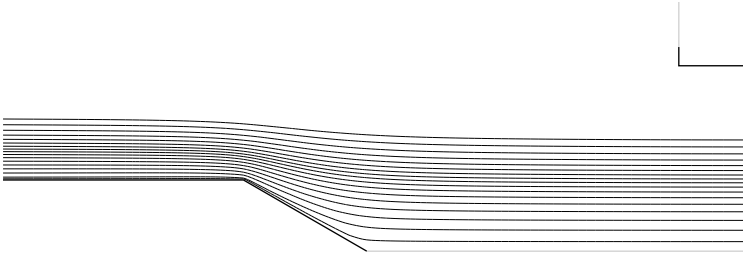

Fig. 8. Streamlines around the train with α=30° outside the tunnel.

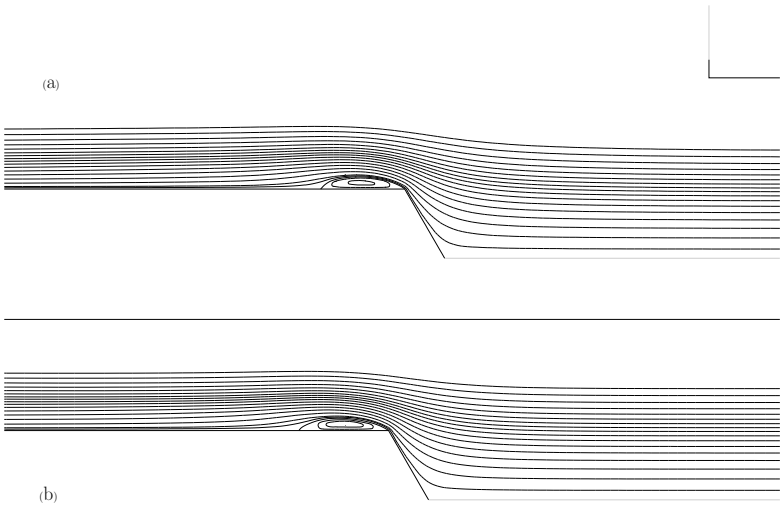

Fig. 9. Streamlines around the train with α=60°: (a) outside and (b) inside the tunnel.

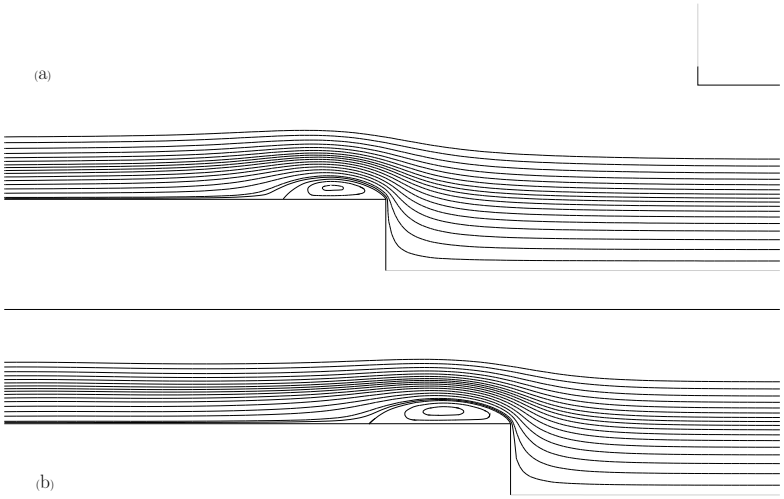

Fig. 10. Streamlines around the train with α=90°: (a) outside and (b) inside the tunnel.

Figure 8 shows the streamlines over the train with α=30° at t=0.003 s. No separation occurs past the nose, even when the train is closer to the portal or inside the tunnel. The other cases (α=60° and 90°) show the presence of a separation bubble (see figures 9 and 10). A first visual inspection supports our choice of sinusoidal shape for the bubble. This region changes only slightly as the train enters the tunnel, as revealed by the images at t=0.003 s (a) and t=0.009 s (b), corresponding to the positions outside and inside the tunnel. The maximum h_b (determined by the streamline defining the reattachment point past the separation region) remains constant while l_b increases by 11% and 29% for α=60° and α=90°, respectively. This phenomenon is caused by

the strong acceleration due to the tunnel blockage effect. l_b adjusts to the new value when the nose is well inside the tunnel, so that $h_b/l_b \approx 1/6$ and $\approx 1/5$ for α=60° and α=90°, respectively. h_b=3.3 mm and 5.9 mm (8.7% and 15.5% of D_{train}) for α=60° and α=90°, respectively. These values only slightly overpredict those in section §3.2 (see figure 11).

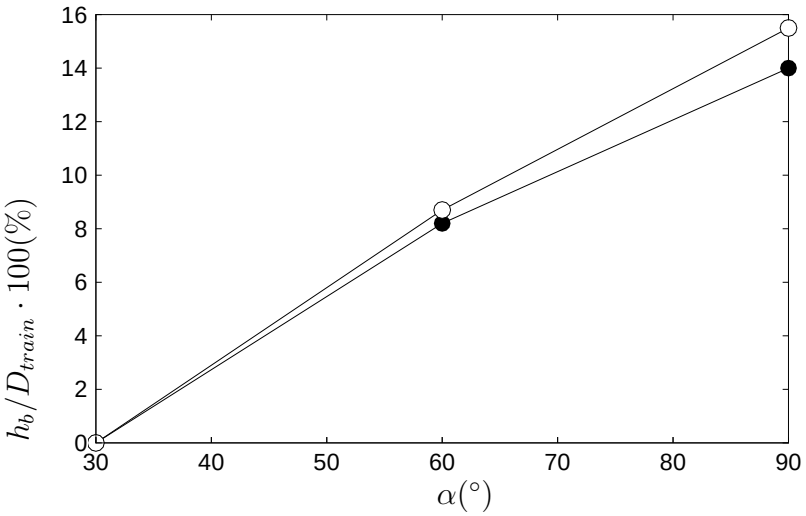

Fig. 11. Percent thickness of separation bubble as function of train nose angle for one- (•) and two-dimensional computations (◦).

4 Results and discussion

4.1 Pressure as the train enters the tunnel

We first investigate the pressure pattern at l=900 mm (see figure 12). The top graph indicates the position of the vehicle head and tail as well as the propagation of the pressure waves at the sound speed. This quantity was determined by measuring the time delay of the pressure signal at different locations (a=345±5 m/s). The lines representing the waves have a steeper gradient than the lines representing the train motion because of the higher velocity. The horizontal line indicates the microphone position. Each intersection of this line with an oblique one corresponds to a major pressure change. The crossing of a compression (resp. expansion) wave is responsible for a pressure growth (resp. attenuation). A wave changes its character from compression to expansion, or vice versa, at a tunnel aperture. Part of its energy is released to the exterior as a micro-pressure wave [10]. The first pressure peak is given by the compression wave C1, which is generated by the train head. After this peak, the intensity

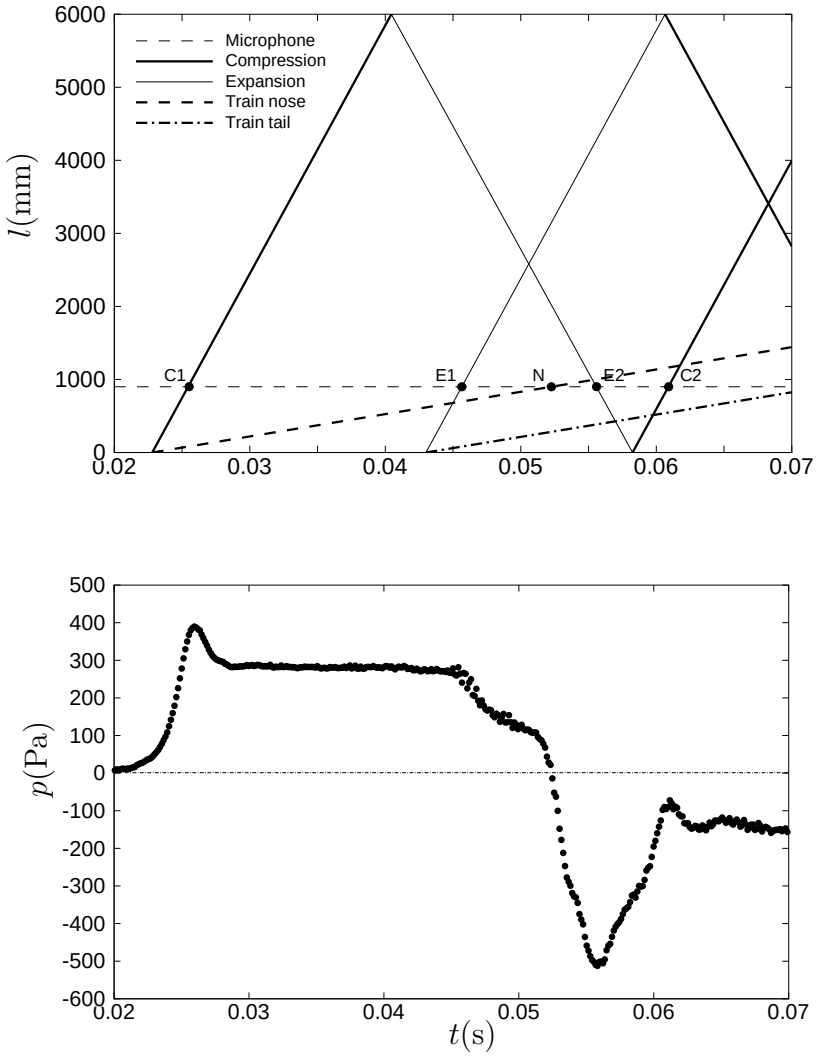

Fig. 12. Pressure at l=900 mm and wave diagram for long train with α=90° travelling at 110 km/h (30.6 m/s). The passage of the waves and train at the microphone location is indicated by black dots in the wave diagram.

decreases at a similar rate as it has increased. A formula exists for computing the maximum pressure rise Δp_{max} induced by a well aerodynamically designed train [48] (also in [49]). Viscous effects are not modelled. The formula reads:

$$\Delta p_{max} = \frac{(1/2)\gamma p_0 M^2(1-\phi^2)}{\phi^2 + M(1-\phi^2) - \gamma M^2(1-\phi^2/2)}, \tag{2}$$

where ϕ=1-β, γ=C_p/C_v and C_p is the specific heat at constant pressure. Five maximum measured pressures are reported in table 1 (p_{meas}) (α=30°) and compared with data given by (2). The estimates are satisfactory given that (2) does not include the influence of the train length.

Table 1

Comparison between initial maximum measured pressures and estimates given by (2) - α=30°, a=345 m/s and γ=1.4.

L_{train} (mm)	V (km/h)	M	p_{meas} (Pa)	Δp_{max} (Pa)	$Err(\%)$
600	63	0.0507	72	67.5	6.6
300	71	0.0572	98	85.6	14.4
300	97	0.0781	160	159.2	0.52
300	113.5	0.0914	226	217.5	3.9
300	135	0.109	306	307	0.32

The pressure trend remains almost constant after the transit of the first compression wave. During this interval, the pressure of the region between the train nose and the rear part of the compression wave is measured. The reduction given by this wave proceeding along the tunnel is counterbalanced by the increase caused by arrival of the train. These effects almost cancel each other. Pressure tends to decrease as the confined region is expanding as the wave travels faster than the train, but, at the same time, the boundary layer along the vehicle brings on a larger effective β. In [5] and [15], the flow given by a train running off-centered with respect to the tunnel axis was studied. An intense pressure rise on the tunnel side closest to the train in correspondence of our interval of almost constant pressure was observed. This may be due to the severe viscous stresses acting in the narrow area.

After this "plateau" region, three events reduce the pressure to an absolute value higher than the first maximum. The sensor detects the expansion wave generated by the train tail entering the tunnel (E1) at $t\approx$0.045 s, the high velocity region around the train nose (N) at $t\approx$0.052 s, and the expansion wave E2 at $t\approx$0.056 s coming from the tunnel exit as a reflection of C1.

The pressure rise at $t\approx$0.06 s is caused by the compression wave C2 appearing when E2 reaches the tunnel entrance. This wave is the transformation of C1 after two reflections at the tunnel apertures. The energy lost either to the exterior, by friction dissipation or by the interaction with other waves and with the train body is negligible during this interval as its intensity is unchanged from the first pressure rise.

4.2 Periodicity of pressure peaks

The periodic pattern after the train has passed the measurement locations is shown in figure 13. The changes produced by the waves (C,D and G,H)

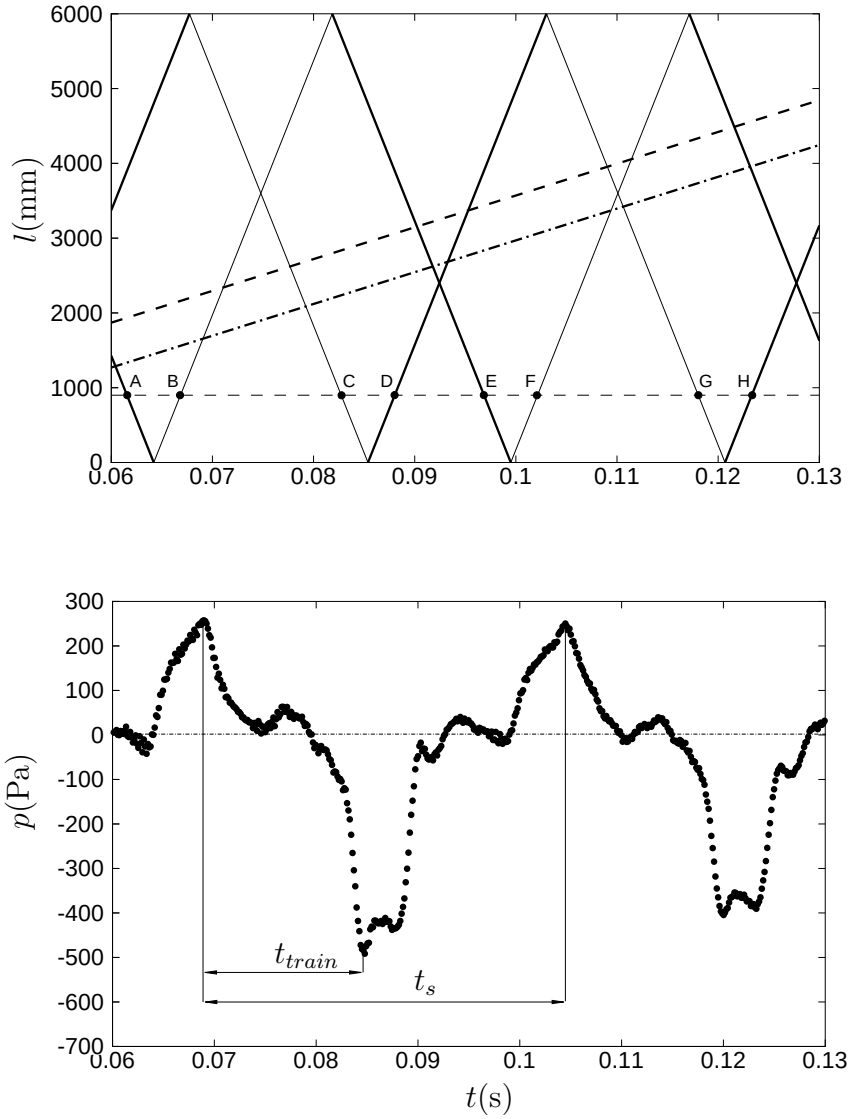

Fig. 13. Periodicity of pressure peaks and wave diagram after the long train with α=60°, V=153 km/h (42.5 m/s) has passed the microphone at l=900 mm. Refer to figure 12 for legend of wave diagram.

originated by C1 (see figure 12) match well with the estimate given by the wave diagram, whereas the transit of the waves related to E1 (A,B and E,F) is predicted in advance by about ∼25 ms. The intensity of the second group of waves is about half of the intensity of the first one, which suggests that any attempt to alleviate the pressure changes should be primarily directed to C1. Compression waves which are reflections of C1 raise the pressure back to the atmospheric value (D and H in figure 13), while the expansion waves C and G reduce the pressure to negative values. The pressure peaks, either positive or negative, are originated by waves coming from the tunnel exit, while waves from the tunnel mouth restore the pressure to the atmospheric value. Other

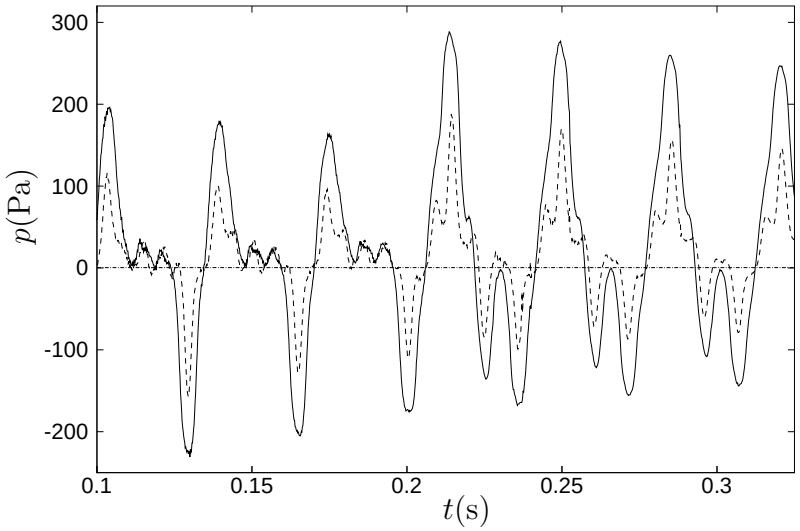

Fig. 14. Pressure peaks at l=300 mm (– –) and l=900 mm (—) after the train has passed all the microphones. Experimental test case of short train with α=30° and V=140 km/h (38.9 m/s).

smaller variations which repeat themselves with regularity are given by smaller waves generated by the main waves interacting with one another or with the train. The pressure pattern is characterized by two time intervals: t_s=0.0355 s is the time taken by a wave to travel L_{tunnel} twice and allows us to calculate $a = 338$ m/s; t_{train} is related to V:

$$t_{train} = \frac{L_{tunnel} - 2l}{a} - \frac{L_{train}}{V}.$$

V=40.9 m/s compares well with the measured value (42.5 m/s).

Figure 14 shows another pressure pattern once the train has passed the microphones. The peaks reduce slightly until t≈0.2 s, when the model emerges from the tunnel exit. The positive peaks become more intense and smaller negative peaks appear. These changes are caused by an expansion wave generated by the nose and a compression one generated by the tail as the train leaves the tunnel. Negative and positive peaks decrease by about 12% and 8% when the train is inside the tunnel, and by about 8% and 5% when it is outside. Indeed, energy is more dissipated in the first case due to the waves interacting with the model, which also results in the production of smaller waves. Full-scale pressure variations reduce at a much faster rate owing to greater viscous stresses on the tunnel surface [50].

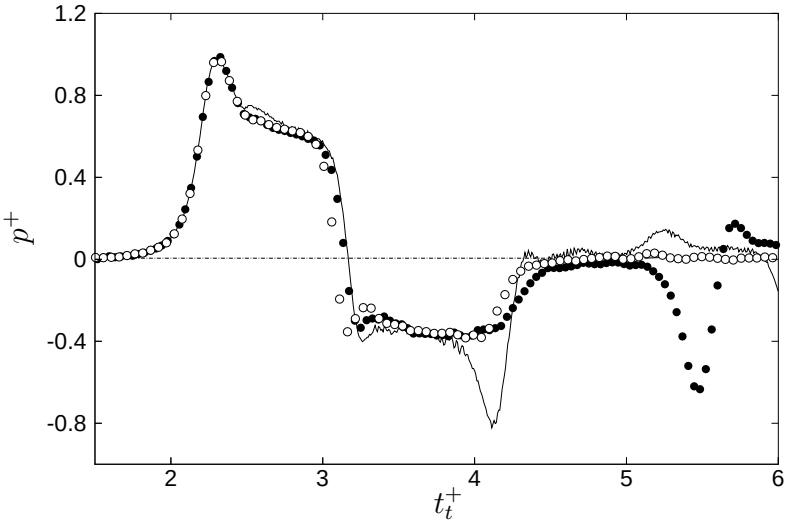

Fig. 15. Scaled pressure for V=61, 104 and 140 km/h (16.9, 28.9 and 38.9 m/s, respectively). Experimental test cases of short model with α=90°. Every three data point is shown for clarity.

4.3 Scaling of pressure pattern

We study the non-dimensional pressure evolution to focus on the influence of the geometrical characteristics. As outlined by [7], we can neglect the Reynolds number effects as this parameter is large. The Mach number effect is not considered because V does not change much and the maximum M is low (M=0.12).

Figure 15 shows the scaled pressure trends at l=300 mm given by the short model with α=90° running at three different velocities. Pressure initially increases with V^2, as suggested by (2). We thus choose to scale the data by $(1/2)\rho_0 V^2$: $p^+=2p/(\rho_0 V^2)$, where ρ_0=1.225 kg/m^3 is the air density outside the tunnel. The time of pressure rise appears to decrease with V, so that $t_t^+=tV/L_{train}$. The curves overlap until $t_t^+\approx$2.5, which supports the hypothesis that the flow is initially purely inviscid, as there is no Reynolds number effect. Scaled-down experiments can thus predict this phenomenon as it occurs in full scale. The maximum value is nearly unity for the flat nose, thus close to the pressure at the train head outside the tunnel, whereas $p^+\approx$0.75 for α=60° and $p^+\approx$0.4 for α=30°. The effect of the boundary layer may be responsible for the small discrepancies when $2.5<t_t^+<4$. The thickest boundary layer (i.e. lowest V) causes the highest pressure in this interval at $t_t^+\approx$2.5, indicating a slightly more pronounced blockage effect. After t_t^+=4, the curves do not superimpose because the train has passed the microphone at l=300 mm and a is now the characteristic kinematic factor.

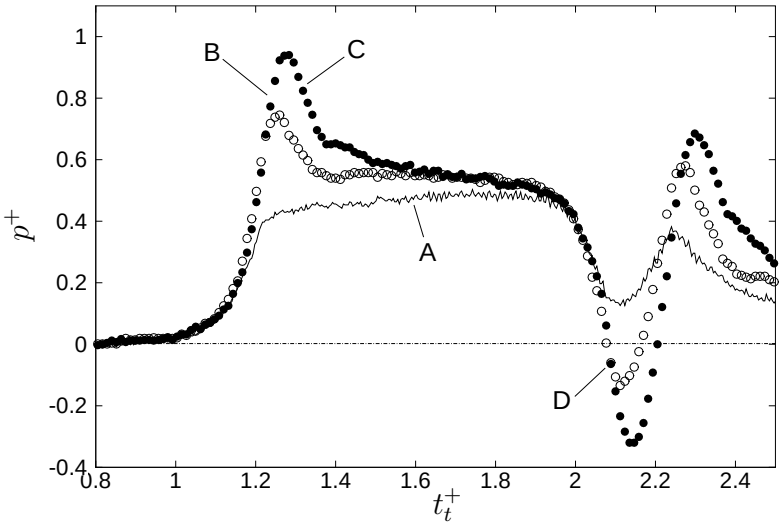

Fig. 16. Influence of nose angle on experimental pressure pattern for long models with circular cross section travelling at 63 km/h (17.5 m/s). α=30° (—), α=60° (○) and α=90° (●). Every three data point is shown for clarity.

4.4 Influence of nose shape

The pressure trends at l=900 mm produced by the long trains with different nose angles are compared in figure 16. A pronounced peak occurs for α>30°, whereas for this angle the pressure increases monotonically, but at a slower rate after the initial rise (A). The peak increases with α because of the stronger recirculation region (B), which effectively increases β. The fluid in front of the train flows toward the train tail through the restricted annular area, it reaches the back of the recirculation region and then decelerates as it encounters a larger area. The pressure suddenly drops because of the low pressure region upwind of the separation bubble (C). The negative peak (D) is then caused by the rarefaction wave originated when the first compression wave arrives at the tunnel exit. More details on the effect of nose shape are found in [11],[14].

The experimental and numerical data are compared. Figure 17 shows the pressure for the train with α=30° (a) and α=60° (b). In the former case, the first pressure rise and the subsequent periodic peaks are well predicted. The slight discrepancy at t≈0.02 s occurs because the code can not simulate the presence of the train until it enters the tunnel. The numerical results slightly overestimate the intensity of the reflected waves, probably on account of the attenuation at the tunnel portals being stronger than that simulated. The peak generated by the recirculation region is also observed in the successive reflections (t≈0.04 s, 0.05 s in figure 17 (b)). The small increment from about -400 to -220 Pa at t≈0.04 s is almost equal to the increase from about 580 to 700 Pa at t≈0.02 s. This suggests that the bubble does not experience significant

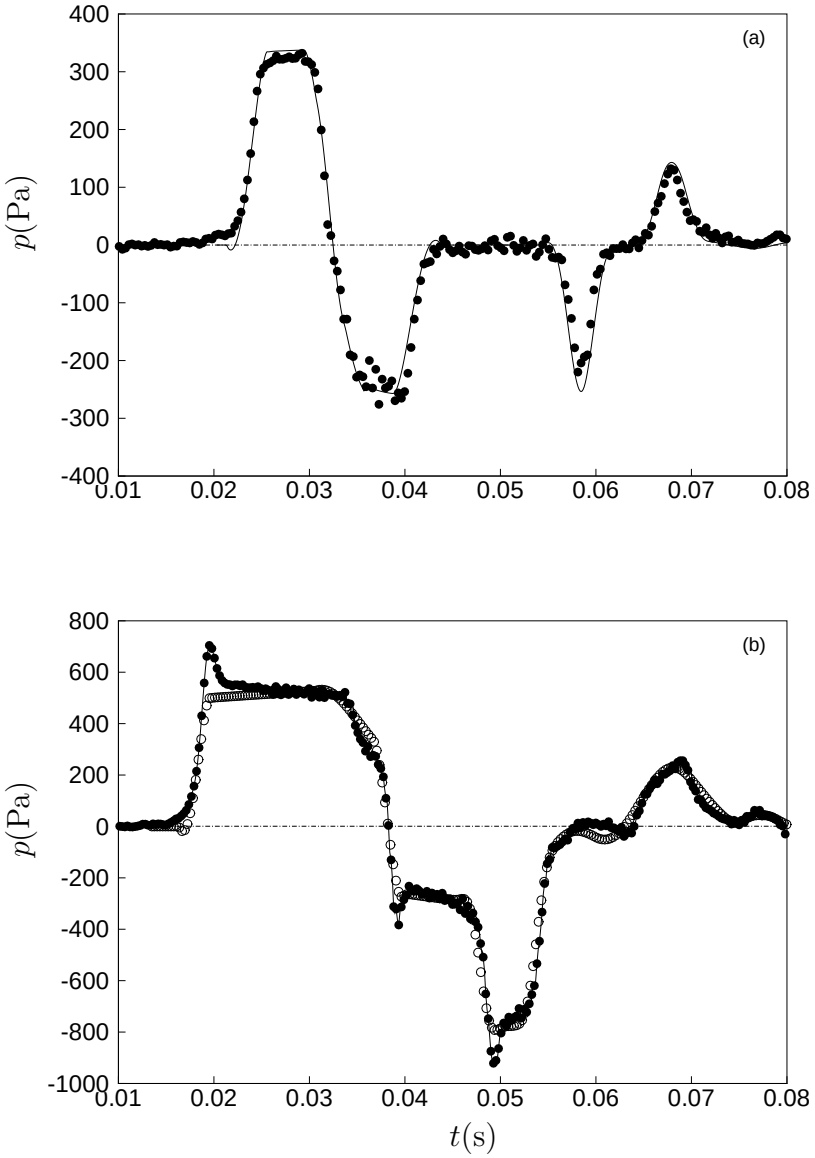

Fig. 17. Comparisons between experimental (•) and numerical data with (—) and without (○) separation bubble model at l=900 mm. Test cases with short model with α=30° and V=140 km/h (38.9 m/s) (a) and with long model with α=60° and V=153 km/h (42.5 m/s) (b). Every other data point is shown for clarity.

modifications after the train has entered the tunnel. The computational trend slightly underestimates the experimental data after the initial pressure rise (t≈0.021 s in figure 17 (b)) probably because the boundary layer behind the bubble is not simulated.

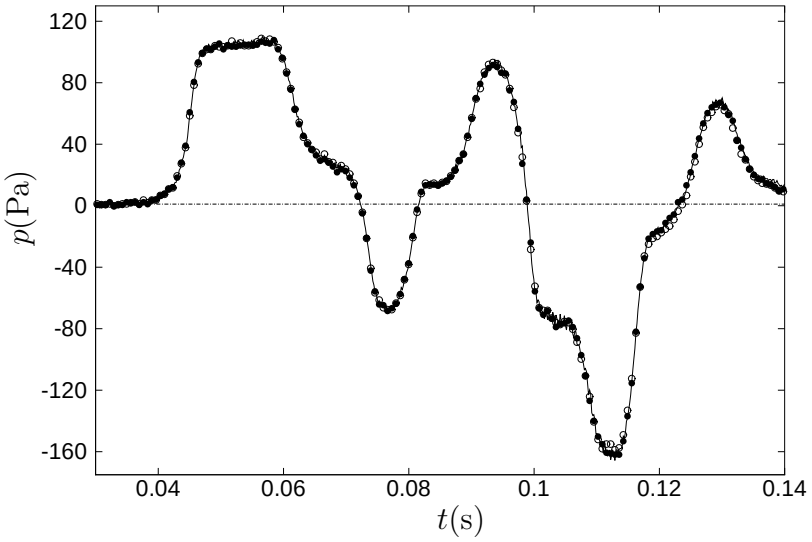

Fig. 18. Comparison amongst pressure patterns at different positions around the tunnel diameter at l=1180 mm: 0° (—), 120° (•), 240° (○). Experimental test cases of short squared-section model travelling at 71 km/h (19.7 m/s). Every four data point is shown for clarity.

4.5 Pressure pattern produced by squared-section train

The pressure induced by the short squared-section train was simultaneously measured at the three points at l=1180 mm (see figure 18). The curves overlap, which indicates that the waves are one-dimensional, as assumed in the numerical calculations. The symmetry is maintained when the train head is aligned with the microphones (t=0.075 s). Figure 19 shows that the squared- and circular-train pressure patterns superimpose during the first increment (t_t^+<3.2) and when viscosity plays a role (3.2<t_t^+<3.8). The cross-sectional shape thus does not influence the initial pressure rise. Similar conclusions were drawn by [15], who compared the flow induced by an axisymmetric model and a ETR500 train model. However, they found a 5% difference in the pressure gradients, which we did not detect. This could be due to the train off-centering with respect to the tunnel axis, which may generate three-dimensional viscous effects.

Theoretical acoustics can be useful to predict the planar character of the pressure waves. These are one-dimensional when the highest frequency of the pressure signal is smaller than a characteristic *cut-off* frequency $f_{c,1}$ of the lowest mode higher than the fundamental mode (one-dimensional planar wave) for L_{tunnel}/D_{tunnel}>10 [51]. Above $f_{c,1}$, transversal waves are induced by a source at a tunnel aperture. In the one-dimensional case, the smallest wavelength is much longer than D_{tunnel} and all the higher modes are attenuated. This occurs when $f_{max}<f_{c,1}=2\pi a/\lambda_1$, where $\lambda_1=2D_{tunnel}$ is the wavelength of the lowest

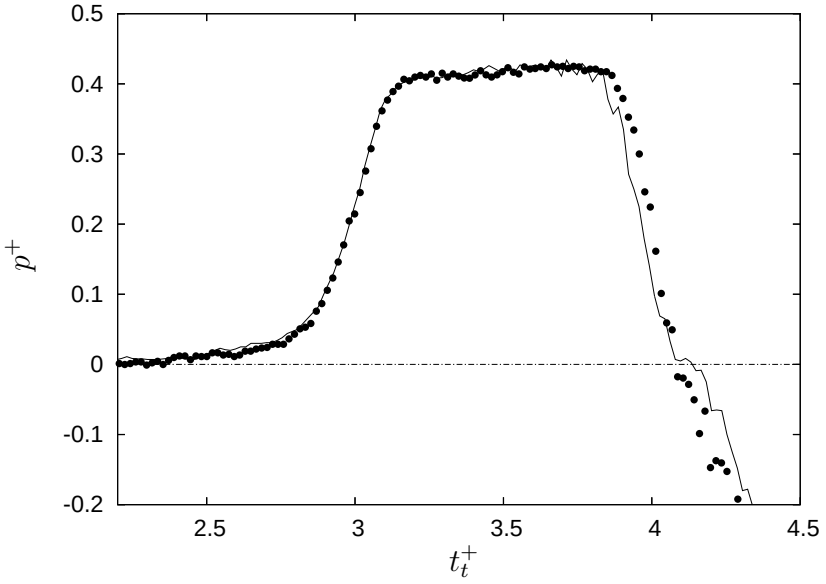

Fig. 19. Comparison between experimental pressure patterns given by short circular train with α=30° (V=141.2 km/h (39.22 m/s)) (—) and short squared train (V=149.4 km/h (41.5 m/s)) (•) at l=900 mm.

higher mode. In our case, $f_{max}\approx$2.5 kHz and $f_{c,1}\approx$11 kHz, so that only planar waves are predicted. Three-dimensional effects are however likely to occur near the tunnel mouth. The analysis by [52] showed that, although the initial transient is one-dimensional, there exists a three-dimensional *steady* pressure field near the entrance.

4.6 Influence of train length

The effect of L_{train} on the initial pressure growth is studied (see figure 20). Although we investigate the pressure during the first instants, we scale the time by L_{tunnel}/a since this quantity does not contain L_{train}, namely t_a^+=ta/L_{tunnel}. The plateau region after the first pressure rise lasts for a longer time for the long train because of the bigger time lag between the first compression wave and the wave from the train tail. The rate of pressure rise in the plateau region is slightly larger for the long train, suggesting the presence of a thicker boundary layer. The initial growth is slightly more intense for the long train ($\sim$6%). This confirms the numerical finding by [30] of an asymptotic maximum as L_{train} increases for a given β and nose shape. Since the flow is subsonic, the entire flow field is influenced by the pressure disturbances. The effect of the low-pressure region around the tail on the first compression wave increases as L_{train} decreases.

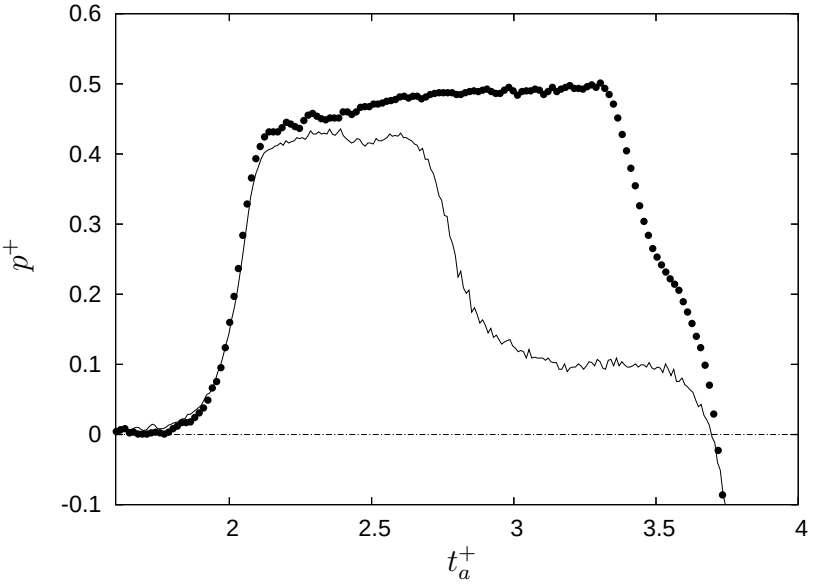

Fig. 20. Influence of train length for squared-section trains at l=900 mm. Experimental test cases with long train running at 94.3 km/h (26.2 m/s) (•) and with short train travelling at 90.7 km/h (25.2 m/s) (—).

4.7 Influence of airshafts

Airshafts are apertures on the tunnel surface serving the purpose of reducing the pressure intensity. Air flows through the apertures, giving substantial reduction of momentum transfer around the train. This in turn leads to drag reduction. Airshafts are appealing for practical applications due to their limited cost, when compared with analogous techniques, such as perforated or flared tunnel hoods [17],[53],[54],[55]. Their design is attractive for easiness of construction and possible modifications. The study by [41] showed that a pressure reduction could be attained when tunnels are connected by open relief ducts. However, the design of such a system is quite involved because of the significant increase in aerodynamic drag and the generation of undesirable cross winds. Airshafts also work to alleviate the intensity of micro-pressure waves [19]. Other studies [25],[56] showed that the effects of tunnel hood windows can be well predicted by the theory of nonlinear sound scattering.

The influence of the airshaft position (l=600, 900 and 1180 mm) on the pressure at l=300 mm is shown in figure 21. The pressure intensity is reduced more when the airshaft is closer to the microphone. Figure 22 shows a schematic of the reflecting waves. An interval of approximately 0.001 s is estimated between two stages of evolution. Full circles denote compression waves and empty circles indicate expansion waves. The circle size represents the wave intensity. At time A (t≈0.025 s), the first wave is aligned with the microphone at l=300 mm and the pressure attains the maximum value. At time B, the compression wave

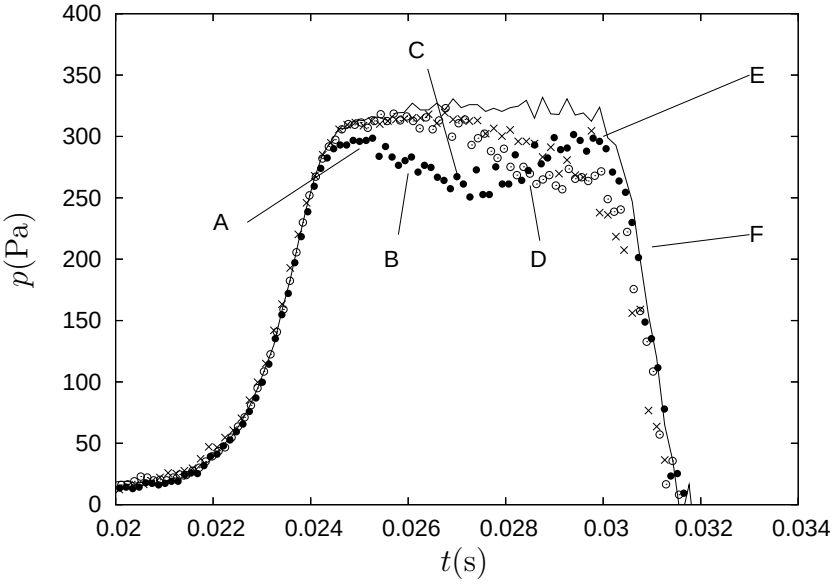

Fig. 21. Influence of distance of airshaft from tunnel entrance on pressure pattern at l=300 mm: no airshaft (—), airshaft at 1180 mm (×), airshaft at 900 mm (○), airshaft at 600 mm (•). Experimental test cases with short squared-section train travelling at 135 km/h (37.5 m/s).

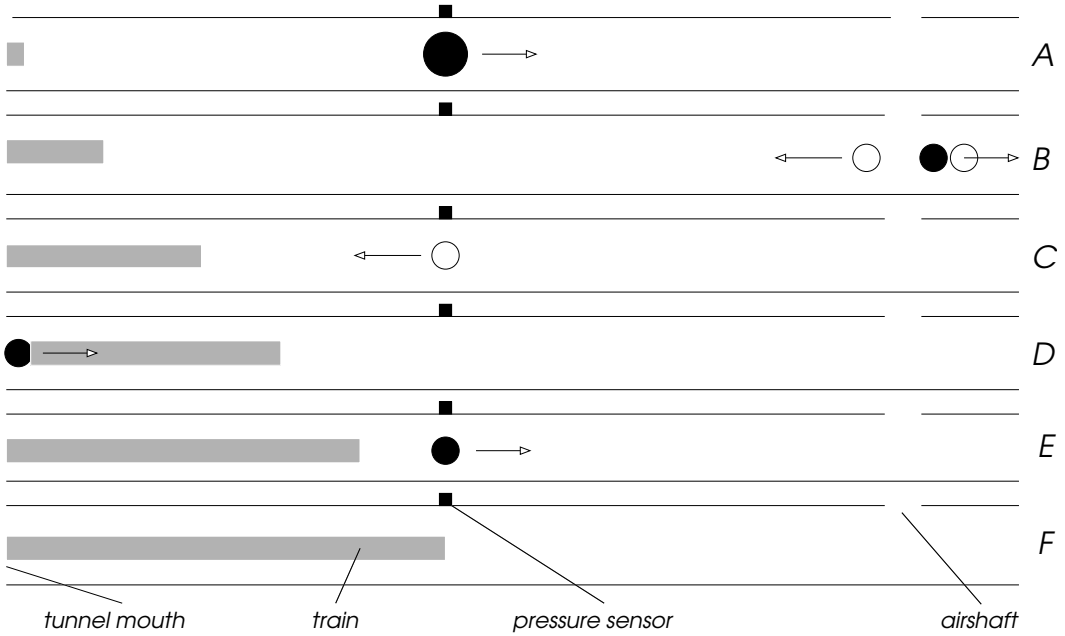

Fig. 22. Schematic of reflecting waves with one airshaft located at l=600 mm (data indicated by • in figure 21).

reaches the airshaft location. Part of the disturbance propagates along, while the rest is reflected as expansion waves both backward to the tunnel entrance and forward to the exit. Pressure drops at the arrival of the small rarefaction wave (C). The disturbance becomes a compression wave (D) and pressure is maximum again at time E. The rates of pressure drop and growth at time C

are very similar, suggesting the passage of the same wave changing its character from rarefaction to compression. The low-pressure high-velocity region around the nose causes the drop at time F. The wave breaks up again when it encounters the airshaft. This process is repeated continuously as smaller waves are generated. The study by [57] shows that a wave encountering an opening can be expressed as an infinite sum of smaller pressure steps, computed by a simple recursive formula.

The intensity of the rarefaction wave generated by the partial reflection of the first compression wave increases with the aperture ratio and thus produces a higher total reduction (see figure 23). The maximum pressure can be reduced by more than 50%, which is slightly higher than the maximum reduction of 40% found by [23]. The energy dissipation, either by viscosity or by the waves interacting with the exterior, is indicated by the second pressure rise being less intense than the first one. Our code is again capable of simulating the flow well, which suggests that two and three dimensional effects are negligible even with airshafts. The pressure trends agree with the one measured by [22]. Lower reductions are expected in real cases because of pressure losses as the tunnel is connected to the exterior by a duct. This effect warrants further analysis through both experiments and numerical simulations.

5 Summary and conclusions

This study was focused on the character of the pressure waves generated by high-speed trains entering a tunnel. We have conducted both experiments in a scaled-down facility and numerical simulations with a one-dimensional code which employed viscous coefficients to provide the required dissipation effects. We have described in detail the initial pressure rise and the pressure pattern once the train has left the confined area. We have confirmed the strong dependence of the pressure peaks on the train velocity and the nose shape, and detected their remarkable periodicity. While the initial growth compares well with full-scale experiments, the subsequent periodic variations are usually much more damped in a real case. This is due to the stronger dissipation effects on the tunnel surface which are not reproduced in the laboratory.

The first aim was to modify our one-dimensional code to account for the influence of the local separation region, which occurs near the train head for high-angled noses. This task can be accomplished by slightly thickening the train body near the nose. The bubble shape was found iteratively until the numerical results matched the experimental data at a satisfactory level. A further analysis of axisymmetric computations confirmed these results.

We have also compared the pressure trends generated by train models with

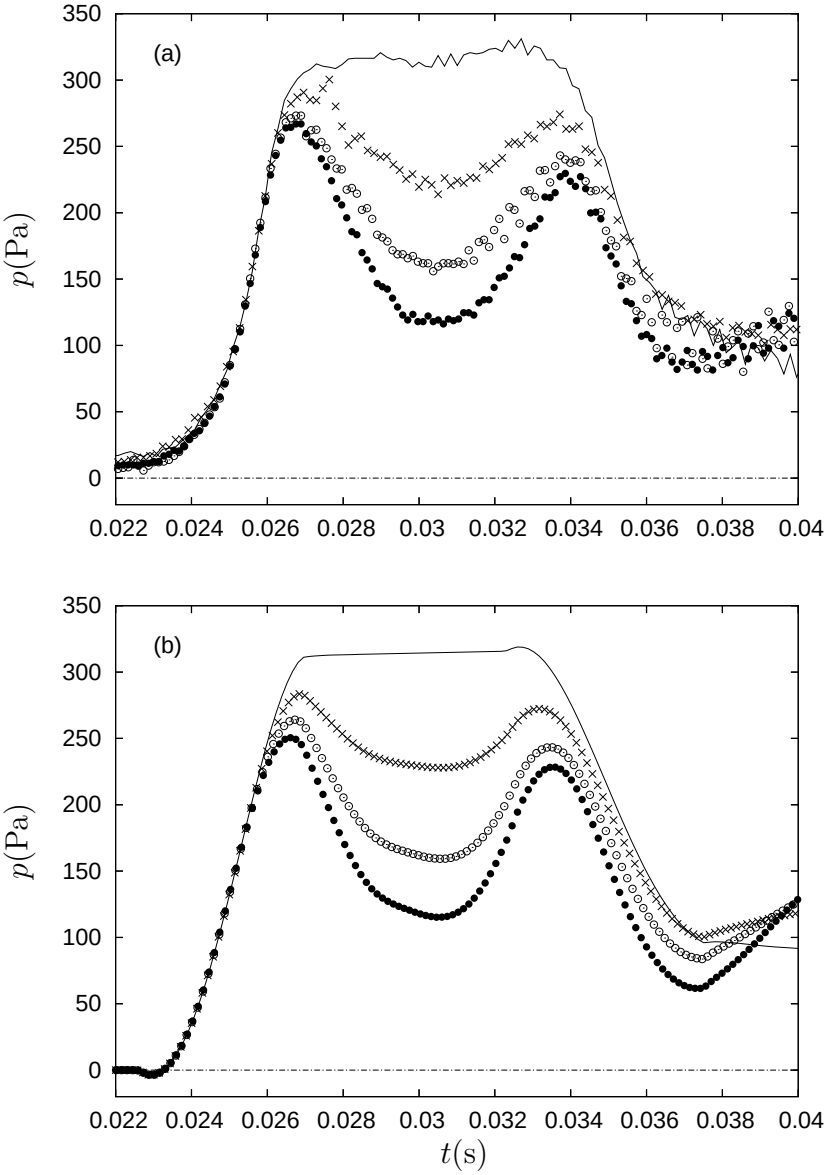

Fig. 23. Influence of number of airshafts located l=1180 mm on the pressure at l=900 mm: none (—), one (×, $\mathcal{A}$=0.04), two (○, $\mathcal{A}$=0.08), three (●, $\mathcal{A}$=0.12). Test cases with short squared-section train travelling at 135 km/h (37.5 m/s): experimental (a) and numerical data (b). Every other numerical data point is shown for clarity.

the same blockage ratio and nose shape, but different cross-sectional shapes. No differences have been found sufficiently downwind, which indicates that the waves are planar and the validity of our one-dimensional code is confirmed. This analysis also suggests that the differences in pressure distributions for an axisymmetric train model and one with a more realistic cross-section found by [15] are due to the viscous effects as the trains are off-centered with respect to the tunnel axis. The fact that the cross-sectional shape is not influential may direct us to the use of one-dimensional models. However, as also [15] claim, the three-dimensional features of full-scale trains must be accounted for in more

challenging studies on friction and form drag.

The third contribution was the study of the effect of the train length on the initial pressure trend. We have shown that the initial peak increases slightly with the train length. This phenomenon is due to the weaker influence of the low-pressure region near the train tail on the head compression wave as the train length increases. The subject deserves further attention as this effect is usually not accounted for in empirical formulas (as the train is considered infinitely long). Our one-dimensional computations also capture well the pressure trends when airshafts are introduced. Increasing the aperture area gives higher pressure reductions (up to $\sim$50%), although the effect quickly saturates.

Acknowledgment

The axisymmetric computations were carried out on the hardware and software resources of CILEA (Consorzio Interuniversitario Lombardo per l'Elaborazione Automatica) in Segrate, Milan.

Nomenclature

Symbol	Definition
a	speed of sound, m/s
A	instantaneous, local free area of tunnel cross section, m^2
$\mathcal{A}$	aperture ratio, between airshaft and tunnel areas, dimensionless
C_{f_g}	skin friction coefficient of the tunnel wall, dimensionless
C_{f_t}	skin friction coefficient of the train wall, dimensionless
C_p	specific heat at constant pressure, J/(kg K)
C_v	specific heat at constant volume, J/(kg K)
D_{train}	diameter of the train model, m
D_{tunnel}	diameter of the tunnel, m
e	internal energy per unit mass, J/kg
E	total energy per unit volume, J/m^3
$\mathbf{f}$	vector of convective fluxes
f	dominant frequency, Hz
f_{max}	maximum frequency generated by train travelling through tunnel, Hz
$f_{c,1}$	cut-off frequency of the lowest mode higher than the fundamental one, Hz
h_b	maximum thickness of the recirculation region past the train nose, m
k	thermal conductivity of air, W/(m K)
l	distance from tunnel entrance, m
l_b	length of recirculation region past the train nose, m
L_{tunnel}	length of tunnel, m
L_{train}	length of train, m
p	pressure, Pa
p_0	atmospheric pressure at standard conditions, Pa
Δp_{max}	initial pressure increment estimated through formula (2), Pa
M	Mach number based on train velocity, $M \equiv V/a$, dimensionless
$\mathcal{P}_g$	perimeter of the tunnel cross section, m
$\mathcal{P}_t$	perimeter of the train cross section, m
$\dot{Q}$	heat power per unit volume, W/m^3
R	ideal gas constant, J/(kg K)
u	air velocity, m/s
u_τ	wall friction velocity on train surface, m/s
$\mathbf{s}$	vector of source terms
t	time, s
t_a^+	time scaled by tunnel length and speed of sound, dimensionless
t_s	time taken by a wave to travel the tunnel length twice, s
t_t^+	time scaled by train velocity and train length, dimensionless
t_{train}	time related to propagation of waves through train velocity, s
T	air temperature, K
$\mathbf{w}$	vector of conservative variables
x	axial coordinate along the tunnel, m
V	train velocity, km/h (m/s)

α	semi-angle of train nose, rad
β	blockage ratio, β=$(D_{train}/D_{tunnel})^2$, dimensionless
γ	ratio of specific heats, dimensionless
λ_1	wavelength of the lowest mode higher than the fundamental one, m
ν	kinematic viscosity of air, m^2/s
Ω	control volume, m^3
ϕ	coefficient ϕ=1-β, dimensionless
ρ	density of air, kg/m^3
ρ_0	density of air at standard conditions, kg/m^3
Σ	surface of the control volume Ω, m^2

References

[1] B. Dayman and D. W. Kurtz, Experimental studies relating to the aerodynamics of trains travelling in tunnels at low speed, *First International Conference on the Aerodynamics and Ventilation of Vehicle Tunnels* (1973).

[2] K. Fujii and T. Ogawa, Aerodynamics of high speed trains passing by each other, *Comput. Fluids*24 (8) (1995), pp. 897–908.

[3] A. E. Vardy, Aerodynamic drag on trains in tunnels. Part 1: Synthesis and definitions, *J. Rail Rapid Tr., Proc IMechE* 210 (1996), pp. 29–38.

[4] A. E. Vardy, Aerodynamic drag on trains in tunnels. Part 2: Prediction and validation, *J. Rail Rapid Tr., Proc IMechE* 210 (1996), pp. 39–49.

[5] T. Ogawa and K. Fujii, Numerical investigation of three-dimensional compressible flows induced by a train moving into a tunnel, *Comput. Fluids* 26 (6) (1997), pp. 565–585.

[6] A. E. Vardy and P Reinke, Estimation of train resistance coefficients in tunnels from measurements during routine operation, *J. Rail Rapid Tr., Proc IMechE* 213 (1999), pp. 71–87.

[7] M. S. Howe and M. Ida and T. Fukuda and T. Maeda, Theoretical and experimental investigation of the compression wave generated by a train entering a tunnel with a flared portal, *J. Fluid Mech.* 425 (2000), pp. 111–132.

[8] T. Ogawa and K. Fujii, Prediction and alleviation of a booming created by a high-speed train moving into a tunnel, *Proc. of the European Community Conference on Computational Methods in Applied Sciences. New York: Wiley* (1996).

[9] T. Aoki and A. E. Vardy and J. M. B. Brown, Passive alleviation of micro-pressure waves from tunnel portals, *J. Sound Vibr.* 220 (5) (1999), pp. 921–940.

[10] A. Baron and P. Molteni and L. Vigevano, High–speed trains: Predictions of micro–pressure wave radiation from tunnel portals, *J. Sound Vibr.* 296 (1-2) (2006), pp. 59-72

[11] T. Maeda and T. Matsumura and M. Iida and K. Nakatani and K. Uchida, Effect of shape of train nose on compression wave generated by train entering tunnel, *The International Conference on Speedup Technology for Railway and Maglev Vehicles, Yokohama, Japan* (1993).

[12] T. Ogawa and K. Fujii, Effect of train shape on a compression wave generated by a train moving into a tunnel, *Proc. of the Shock Wave Symposium, Chiba, Japan* (1994).

[13] M. S. Howe, Review of the theory of the compression wave generated when a high-speed train enters a tunnel, *Proc. Instn. Mech. Engrs.* 213 - Part F (1999).

[14] H. Kwon and K. Jang and Y. Kim and K. Yee and D. Lee, Nose shape optimization of high-speed train minimization of tunnel sonic boom, *JSME International J. Series C-Mechanical Systems Machine Elements and Manufacturing*44 (3) (2001), pp. 890–899.

[15] M. Bellenoue and V. Moriniére and T. Kageyama, Experimental 3-D simulation of the compression wave, due to train-tunnel entry, *J. Fluids Struct.* 16 (2002), pp. 581–595.

[16] Ozawa, T. and Maeda, T. and Matsumura, T. and Uchida, K. Kajiyama, H. and Tanemoto, K, Counter-measures to reduce micro-pressure waves radiating from the exits of Shinkansen tunnels, *Seventh International Conference on the Aerodynamics and Ventilation of Vehicle Tunnels* (1991).

[17] M. S. Howe, The compression wave generated by a high-speed train at a vented tunnel entrance, *J. Acoust. Soc. Am.* 104 (3) (1998), pp. 1158–1164.

[18] M. Bellenoue and B. Auvity and T. Kageyama, Blind hood effects on the compression wave generated by a train enetring a tunnel, *Exp. Th. Fluid Sc.* 25 (2001), pp. 397–407.

[19] T. S. Yoon and S. Lee and J. H. Hwang and D. H. Lee, Prediction and validation on the sonic boom by a high-speed train entering a tunnel, *J. Sound Vibr.* 247 (2) (2001), pp. 195–211.

[20] J. M. B. Brown and A. E. Vardy, Reflections of pressure waves at tunnel portals, *J. Sound Vibr.* 173 (1) - Part F (1994), pp. 95–111.

[21] A. E. Vardy, The use of airshafts for the alleviation of pressure transients in tunnels, *Second ISAVVT Paper C4, BHRA, Cambridge, UK,* (1976).

[22] R. G. Gawthorpe and C. W. Pope, Reduced cross sections for high-speed tunnels in shallow ground using airshafts, *International Conference on Speedup Technology for Railway and Maglev Vehicles* (1993), pp. 185–190.

[23] J. Burri and F. Zumsteg, Airshafts for the alleviation of pressure waves in tunnels of the New Swiss Rail, *Ninth International Conference on the Aerodynamics and Ventilation of Vehicle Tunnels* (1997), pp. 289–299.

[24] D. A. Henson and C. W. Pope, The alleviation of pressure transients in a main line railway tunnel, *Ninth International Conference on the Aerodynamics and Ventilation of Vehicle Tunnels* (1997), pp. 849–862.

[25] M. S. Howe, On the role of separation in compression wave generation by a train entering a tunnel hood with a window, *IMA J. Appl. Math.* (2005), pp. 400–418.

[26] A. E. Vardy, Initial emergency ventilation in a twin-track tunnel, *First International Conference on Safety in Road and Rail Tunnels, Basel, Switzerland* (1992), pp. 127–134.

[27] A. E. Vardy, Model based predictive control of road tunnel portal emissions, *ITA World Tunneling Congress on Reclaiming the Underground Space, Amsterdam, The Netherlands,* $12^{th} - 17^{th}$ *April. Ed: J. Saveur - International Tunnelling Association Vol. 1*70 (2003), pp. 207–212.

[28] The limit of rapid transit, *Scientific American* 101 (1909), p. 366.

[29] V. Bourquin and M. Mossi, *Rapport Final - Etude Principal- Groupe Mécanique, Rapport Swissmetro EPFL 1.0111/1.6210/a, Lausanne* (1998), pp. 581–595.

[30] T. Ogawa and K. Fujii, Numerical simulation of compressible flows induced by a train moving into a tunnel, *Comp. Fluid Dyn. J.* 3 (1) (1994), pp. 63–82.

[31] T. Johnson, 1/25 Scale moving model tests for the TRANSAERO project, *TRANSAERO Symposium (Transient Aerodynamics Railway System Optimization, Paris, France)* (1999).

[32] B. Dayman and A. E. Vardy, *Seventh International Conference on the Aerodynamics and Ventilation of Vehicle Tunnels* (1991), pp. 757–787.

[33] W. B. de Wolf and E. A. Demmenie, A new test facility for the study of interacting pressure waves and their reduction in tunnels for high-speed trains, *Ninth International Conference on the Aerodynamics and Ventilation of Vehicle Tunnels* (1997), pp. 301–316.

[34] E. A. Demmenie and A. C. De Bruin and E. Klaver, Experimental pressure wave research at NLR for high-speed rail tunnels, *Report of the National Aerospace Laboratory NLR, No. NLR-TR-98375* (1998).

[35] R. Grégoire and J. M. Rety and F. Masberbat and V. Morinière and M. Bellenoue and T. Kageyama, Experimental study (scale $1/70^{th}$) and numerical simulation of the generation of pressure waves and micro-pressure waves due to high-speed train-tunnel entry *Ninth International Conference on the Aerodynamics and Ventilation of Vehicle Tunnels* 27 (1997), pp. 877–903.

[36] B. Auvity and T. Kageyama, Etude expérimentale et numérique de l'onde de compression générée par l'entrée d'un train dans un tunnel *Comptes Rendus de l'Académie des Sciences, Paris, t. 323, Séries IIb, Mécanique des Fluides* (1996), pp. 87–94.

[37] Arts, T., Measurements techniques in fluid dynamics - an Introduction, *VKI - Lecture series - LS 1994-01* (1994).

[38] D. J. Tritton, Physical Fluids Dynamics, *Oxford Science Publications - Second Edition* (1988).

[39] G. K. Batchelor, An Introduction to Fluid Dynamics, *Cambridge University Press* (1967).

[40] A. Jameson and W. Schmidt and E. Turkel, Numerical solutions of the Euler equations by finite volume methods using Runge–Kutta time–stepping schemes, *AIAA Fifth Computations Fluid Dynamics Conference, 81–1259* (1981).

[41] A. Baron and P. Mossi and S. Sibilla, The alleviation of the aerodynamic drag and wave effects of high-speed trains in very long tunnels, *J. Wind Eng. Ind. Aero.* 89 (2001), pp. 365–401.

[42] I. E. Idelchik, Handbook of Hydraulic Resistance, *Hemisphere Publishing Corporation,* Second edition (1986).

[43] R. G. Gawthorpe and C. W. Pope, The measurement and interpretation of transient pressures generated by trains in tunnels, *Second International Conference on the Aerodynamics and Ventilation of Vehicle Tunnels* (1976), pp. 35–54.

[44] H. Glöcke and P. Pfretzschner, High speed tests with ICE/V passing through tunnels and the effect of sealed coaches on passenger comfort, *Sixth International Conference on the Aerodynamics and Ventilation of Vehicle Tunnels* (1988), pp. 23–44.

[45] G. Mancini and A. Malfatti, Full scale measurements on high–speed train ETR 500 passing in open air and in tunnels of Italian high–speed line, *TRANSAERO - A European Initiative on Transient Aerodynamics for Railway System Optimisation, ed. B. Schulte–Werning, R. Grégoire, A. Malfatti, G. Matschke.* Volume 79 of Notes on Numerical Fluid Mechanics and Multidisciplinary Design, Springer–Verlag, Berlin (2002), pp. 101–122.

[46] W. A. Woods and C. W. Pope, On the range of validity of simplified one dimensional theories for calculating unsteady flows in railway tunnels, *Third International Conference on the Aerodynamics and Ventilation of Vehicle Tunnels* (1979), pp. 115–148.

[47] A. E. Vardy and B. Dayman, Alleviation of tunnel entry pressure transients: 2. Theoretical modelling and experimental correlation, *Third International Conference on the Aerodynamics and Ventilation of Vehicle Tunnels* (1979), pp. 363–373.

[48] K. Matsuo and T. Aoki and S. Mashimo and E. Nakastu, Entry compression wave generated by a high-speed train entering a tunnel, *Ninth International Conference on the Aerodynamics and Ventilation of Vehicle Tunnels* (1997).

[49] W. A. Woods and C. W. Pope, Secondary aerodynamic effects in rail tunnels during vehicle entry, *Second International Conference on the Aerodynamics and Ventilation of Vehicle Tunnels* (1976), pp. 71–86.

[50] W. A. Woods and C. W. Pope, A generalised flow prediction method for the unsteady flow generated by a train in a single-track tunnel, *J. Wind Eng. Ind. Aero.* 7 (1981), pp. 331–360.

[51] P. M. Morse and K. U. Ingard, Theoretical Acoustics, *McGraw-Hill Book Company* (1968).

[52] Sugimoto, N. and Ogawa, T., Acoustic analysis of the pressure field in a tunnel, generated by the entry of a train, *Proc.: Mathematical, Physical and Engineering Sciences*454 (1976) (1998), pp.2083–2112.

[53] M. S. Howe, Prolongation of the rise time of the compression wave generated by a high-speed train entering a tunnel, *Proc. R. Soc. London A* 455 (1999), pp. 863–878.

[54] M. S. Howe, On the compression wave generated when a high-speed train enters a tunnel with a flared portal, *J. Fluids Struct.* 13 (1999), pp. 481–498.

[55] J. K. Mok and J. Yoo, Numerical study on high speed train and tunnel interaction, *J. Wind Eng. Ind. Aero.* 89 (2001), pp. 17–29.

[56] M. S. Howe and M, Iida and T. Fukuda and T. Maeda, Aeroacoustics of a tunnel-entrance hood with a rectangular window, *J. Fluid Mech.* 487 (2003), pp. 211–243.

[57] B. Auvity and M. Bellenoue, Effects on an opening on pressure wave propagating in a tube, *J. Fluid Mech.* 538 (2005), pp. 269–289.

List of Figures

23 Influence of number of airshafts located l=1180 mm on the pressure at l=900 mm: none (—), one (×, $\mathcal{A}$=0.04), two (∘, $\mathcal{A}$=0.08), three (•, $\mathcal{A}$=0.12). Test cases with short squared-section train travelling at 135 km/h (37.5 m/s): experimental (a) and numerical data (b). Every other numerical data point is shown for clarity. 27